SCIENCE CHINA
Chemistry

•ARTICLES•
SPECIAL ISSUE: 2022 Emerging Investigator Issue

November 2022 Vol.65 No.11: 2205–2213
https://doi.org/10.1007/s11426-022-1324-0

Surface coatings of two-dimensional metal-organic framework nanosheets enable stable zinc anodes

Liling Lei[1], Feifan Chen[1], Yulun Wu[1], Jian Shen[2,3], Xue-Jun Wu[1], Shishan Wu[1*] & Shuai Yuan[1*]

[1]*State Key Laboratory of Coordination Chemistry, School of Chemistry and Chemical Engineering, Nanjing University, Nanjing 210093, China;*
[2]*National and Local Joint Engineering Research, Center of Biomedical Functional Materials, School of Chemistry and Materials Science, Nanjing Normal University, Nanjing 210023, China;*
[3]*Jiangsu Engineering Research Center of Interfacial Chemistry, Nanjing University, Nanjing 210093, China*

Received April 29, 2022; accepted June 30, 2022; published online September 8, 2022

Aqueous zinc-ion batteries (ZIBs) have been considered as safe and scalable energy storage solutions, but the dendrite and corrosion issues of Zn anodes have hindered their further application. Herein, we demonstrate that two-dimensional metal-organic framework (MOF) nanosheets can act as protective coatings to prevent dendrite formation and hydrogen evolution of Zn anodes. The morphology of MOFs was tuned from octahedral nanoparticles (UiO-67-3D) to nanosheets (UiO-67-2D), leading to significantly enhanced protective performance. UiO-67-2D nanosheets-coated Zn anodes displayed smaller polarization, longer cycling lifetime and lower H_2 evolution than those of UiO-67-3D nanoparticles in symmetrical cells, which has been attributed to the higher concentration of surface Zr-OH/H_2O to induce uniform Zn deposition and one-dimensional (1D) channels perpendicular to the Zn surface to regulate Zn^{2+} diffusion. The assembled UiO-67-2D@Zn||Mn_2O_3/C full cell shows a high capacity of 240 mAh g^{-1} at 1 A g^{-1} and excellent cycling stability.

metal-organic frameworks, nanosheets, zinc-ion battery, zinc anode

Citation: Lei L, Chen F, Wu Y, Shen J, Wu XJ, Wu S, Yuan S. Surface coatings of two-dimensional metal-organic framework nanosheets enable stable zinc anodes. *Sci China Chem*, 2022, 65: 2205–2213, https://doi.org/10.1007/s11426-022-1324-0

1 Introduction

Aqueous zinc-ion batteries (ZIBs) are promising candidates for large-scale energy storage systems owing to their high specific capacity (theoretical weight capacity of 820 mAh g^{-1} and volume capacity of 5,855 mAh cm^{-3}), low cost, inherent safety, and environmental benignity of Zn [1–4]. However, the application of ZIBs has been seriously hindered by dendrite growth (resulting from nonuniform Zn deposition) [5], hydrogen evolution reaction (HER) (caused by thermodynamic instability of Zn in aqueous electrolytes) [6] and corrosion (self-corrosion and electrochemical corrosion) [7]. To address these challenges, several strategies have been proposed through the optimization of electrolytes [8], design of porous Zn anodes [9,10], and surface modification by protective coatings [11]. Among these strategies, surface modification by protective coatings has been shown to enhance the cycling stability of Zn anode by regulating the Zn^{2+} diffusion, creating uniform nucleation sites, and isolating the Zn surface from corrosive aqueous electrolytes [12–14]. Various organic and inorganic materials have been attempted as protective layers of Zn anodes, such as organic polymers [15], carbon materials [16], metal oxides [17–19], and metal sulfides [20]. For example, modification of Zn surface with carbon has been shown to facilitate homogeneous current distribution and uniform Zn deposition [21]. However, the

*Corresponding authors (email: syuan@nju.edu.cn; shishanwu@nju.edu.cn)

conductive nature of carbon coating promotes the Zn deposition and dendrite formation on the carbon surface, posing a threat to long-term cycling. Non-conductive layers, such as ZrO_2 [17], TiO_2 [18], Al_2O_3 [19], HfO_2 [22], and ZnO [23], which show significant inhibitory effects on dendrite formation and adverse reactions, have been explored. Nevertheless, the electrochemically inert layers may hinder the ion/electron transport and reduce the rate performance of protected Zn anodes. Therefore, electrically insulating and ionically conductive materials are highly desired as protective materials for Zn anodes, and metal-organic frameworks (MOFs) are suitable candidates.

MOFs are porous crystalline materials constructed from inorganic metal nodes and organic linkers [24]. Compared with other organic and inorganic materials, such as organic polymers and metal oxides, MOFs exhibit the following merits in stabilizing Zn metal anodes. Firstly, the intrinsic pores of MOFs allow facile diffusion of Zn^{2+}, while their insulating nature ensures the deposition of Zn under the MOF-protective layers. Secondly, the surface structure of MOFs can be judiciously tuned to regulate the interaction between Zn surface and electrolytes. The precisely defined crystal structure of MOFs further facilitates the understanding of the structure-property relationship to guide the rational design of Zn coatings. Finally, the morphology of MOFs can be controlled to form stable two-dimensional films attaching to the Zn surface. By engineering the surface of MOFs, we expect to realize uniform Zn nucleation and retard side reactions. Despite the aforementioned merits, only a handful of MOFs have been explored as protective coatings of Zn anodes, including ZIF-8 [25–29], HKUST-1 [30], UiO-66 [31], ZIF-7 [32], and Zn-BTC [33]. Although these works highlight the promise of MOFs as Zn anode coatings, these MOFs are usually obtained as nanoparticles and deposited onto Zn anodes without structural or morphological design.

Herein, we synthesized two MOFs, namely UiO-67-3D and UiO-67-2D, and studied the effect of structures and morphologies on their performance as Zn anode coatings. UiO-67-3D has a three-dimensional (3D) framework structure forming octahedral nanoparticles, whereas UiO-67-2D is a two-dimensional (2D) network with a nanosheet morphology. Coating UiO-67-2D layers on the Zn anode dramatically reduced the polarization (overpotential of 50 mV at 3 mA cm^{-2}) and elongated the cycling lifetime (850 h at 0.5 mAh cm^{-2}), while the overpotential of UiO-67-3D@Zn anode increased rapidly within 210 h under the same cycling condition. Furthermore, *in situ* gas chromatography-mass spectrometry (GC-MS) studies revealed that UiO-67-2D nanosheets-coated Zn anodes displayed lower hydrogen evolution (<0.5 mmol h^{-1} cm^{-2}) than UiO-67-3D (1.1 mmol h^{-1} cm^{-2}) and bare Zn (2.6 mmol h^{-1} cm^{-2}) in symmetrical cells, which is in agreement with the coulombic efficiency (CE) measurements. The superior protective performance of UiO-67-2D compared with UiO-67-3D was attributed to the higher concentration of surface Zr-OH/H_2O groups as zincophilic sites to allow uniform Zn nucleation, which was confirmed by density functional theory (DFT) calculations, diffuse reflectance infrared Fourier transform spectroscopy (DRIFTS), thermogravimetric analysis (TGA), and contact angle measurements. Besides, the parallel orientation of UiO-67-2D nanosheets on the Zn surface vertically aligns the MOF channels, which regulates Zn diffusion, leading to dendrite-free Zn deposition. The good performance of UiO-67-2D@Zn anode was further verified in a UiO-67-2D@Zn||Mn_2O_3/C cell showing high capacity (240 mA h g^{-1} at 1 A g^{-1}) and excellent cycling stability (~100% CE and 81% capacity retention after 1,500 cycles at 2 A g^{-1}), which is much better than those of UiO-67-3D@Zn||Mn_2O_3/C and bare Zn||Mn_2O_3/C. This work highlighted the impact of MOF structures/morphologies on the Zn anode performance to guide the rational design of protective coatings for stable Zn anodes.

2 Results and discussion

2.1 Synthesis of UiO-67-3D nanoparticles and UiO-67-2D nanosheets

To overcome the challenges of Zn anodes in dendrite formation and parasitic HER (Figure 1a), two MOFs with the same metal and ligand but different morphologies were selected. UiO-67-3D [34] formed octahedral nanoparticles, similar to previously reported MOF materials used as protective coatings of Zn anodes (Figure 1b inset) [25–33]. On the other hand, taking advantage of the high tunability of MOFs, 2D nanosheets were obtained, namely UiO-67-2D (Figure 1c inset) [35,36]. We propose that UiO-67-2D nanosheets may form denser layers than UiO-67-3D nanoparticles to regulate the diffusion of Zn^{2+} (Figure 1b, c). Meanwhile, the exposed Zr-OH/H_2O on the surface of UiO-67-2D nanosheets may provide nucleation sites for uniform Zn deposition.

By judiciously controlling the Zr^{4+}/BPDC (BPDC = biphenyl-4,4′-dicarboxylate) ratio and reaction temperature during the MOF-synthesis, UiO-67-3D and UiO-67-2D were successfully isolated. The structures of UiO-67-3D and UiO-67-2D were confirmed by power X-ray diffraction (PXRD) patterns, which matched well with the simulations based on the reported crystal structures (Figure 2b) [34–36]. UiO-67-3D is formed by connecting $[Zr_6(\mu_3\text{-}O)_4(\mu_3\text{-}OH)_4](CO_2)_{12}]$ clusters with 12 linear BPDC linkers into a 3D framework (Figure 2a, Figure S1a, Supporting Information online). On the other hand, UiO-67-2D has 2D network structures with $[Zr_{12}(\mu_3\text{-}O)_8(\mu_3\text{-}OH)_8(\mu_2\text{-}OH)_6](OH)_6(H_2O)_6(CO_2)_{12}$ cluster (Figure 2a, Figure S1b). Each Zr_{12}-cluster is coordinated to

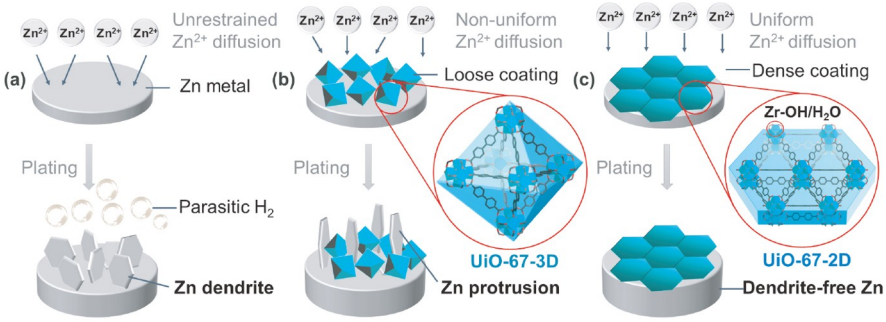

Figure 1 Scheme of anode surface evolution during plating/stripping for bare Zn suffering from dendrite growth and parasitic H_2 (a), UiO-67-3D@Zn exhibiting non-uniform Zn^{2+} diffusion and Zn protrusion (b), and UiO-67-2D@Zn-coated Zn showing uniform Zn^{2+} diffusion and dendrite free plating/stripping (c). Insets show the crystal structure of UiO-67-3D and UiO-67-2D with surface Zr-OH/H_2O groups (color online).

12 carboxylate groups from BPDC linkers within the equatorial position, and terminated by six pairs of -OH/H_2O on the top and bottom. UiO-67-3D and UiO-67-2D exhibit different porosities, as confirmed by the N_2 sorption isotherms at 77 K (Figure 2c). Brunauer-Emmett-Teller (BET) surface area of UiO-67-3D and UiO-67-2D was calculated to be 2,450 and 424 $m^2 g^{-1}$, matching the literatures [34–36]. Pore size distributions derived from N_2 adsorption isotherms reveal the pore sizes of 1.2 and 0.8 nm for UiO-67-3D and UiO-67-2D (Figure 2c inset), respectively, corresponding to the octahedral cages and triangular channels in the crystal structures of UiO-67-3D and UiO-67-2D (Figure 1). These results confirmed the successful synthesis of UiO-67-3D and UiO-67-2D.

The morphologies of UiO-67-3D and UiO-67-2D were characterized by scanning electron microscopy (SEM). UiO-67-3D forms uniform octahedral nanoparticles with an average size of ~300 nm (Figure 2d). In contrast, UiO-67-2D are nanoplates with an average edge size of ~200 nm (Figure 2e). The orientation of UiO-67-2D was further revealed by high-resolution transmission electron microscopy (HR-TEM). The hexagonal lattices can be clearly observed along the *c*-axis (Figure 2f, g), indicating that the UiO-67-2D nanosheets were grown within the *ab*-plane perpendicular to the *c*-axis. The triangular channels are aligned perpendicular to the nanosheets. The lattice fringe in HR-TEM images matchs well with the crystal structures of UiO-67-2D (Figure 2g inset). This structural model agrees with the PXRD patterns of UiO-67-2D, in which the diffraction peaks of (00*l*) families were absent due to the low dimension along the *c*-axis.

2.2 Fabrication of UiO-67-3D- and UiO-67-2D-coated Zn anodes

UiO-67-3D- and UiO-67-2D-coated Zn anodes were prepared by drop-casting a suspension of MOF particles onto a polished Zn foil. UiO-67-3D and UiO-67-2D remain stable and crystalline after depositing onto Zn anodes, as confirmed by their characteristic diffraction peaks in PXRD (Figure 3a). SEM image of UiO-67-3D@Zn shows loosely packed UiO-67-3D nanoparticles on the surface without preferred orientations (Figure 3b). In contrast, UiO-67-2D nanosheets are parallelly stacked forming a denser protective layer (Figure 3c). Cross-section SEM images indicate the similar thickness (~20 μm) of UiO-67-3D and UiO-67-2D layers on the Zn surface (Figure 3d, f). The position of UiO-67-3D and UiO-67-2D layers on the Zn foil was further confirmed by elemental mapping images with energy dispersive X-ray spectrometry (EDS). A clear layering of Zn and Zr elements was observed, in which Zr mainly existed in the MOF-based surface coating layer (Figure 3e, g) on the top of the Zn foil.

The porous MOF coatings exhibit poor electronic conductivity, but high ionic conductivity and high Zn^{2+} transference number, enabling them as sturdy artificial solid electrolyte interphase layers. The ionic conductivity was calculated from electrochemical impedance spectroscopy (EIS) using symmetrical cells (Figure S2). The slightly higher ionic conductivity of UiO-67-2D (2.65×10^{-3} S cm^{-1}) than UiO-67-3D (1.13×10^{-3} S cm^{-1}) can be attributed to its 1D open channels aligned perpendicular to the Zn surface. On the other hand, the Zn^{2+} transference number of the UiO-67-2D reaches 0.84, which is higher than that of bare Zn (0.31) and UiO-67-3D (0.65, Figure S3), promising for more effective Zn^{2+} conduction. The enhanced Zn^{2+} transference number of UiO-67-2D can be related to its small and well-oriented channels which allow fast Zn^{2+} transportation while block the SO_4^{2-} anions. The selective binding of SO_4^{2-} anions by Zr-OH/H_2O of MOFs further inhibits the transport of SO_4^{2-} anions as demonstrated previously [37].

To study the effect of different MOF coatings on the Zn stripping/plating behavior, MOFs@Zn electrodes symmetric cells were assembled where the rate performance of Zn, UiO-67-3D@Zn, and UiO-67-2D@Zn electrodes was measured at various current densities (Figure 4a). The UiO-67-2D@Zn electrode displays low overpotential and stable voltage profiles. With the current density increasing from 0.25 to 3 mA cm^{-2}, the Zn symmetric cell with UiO-67-

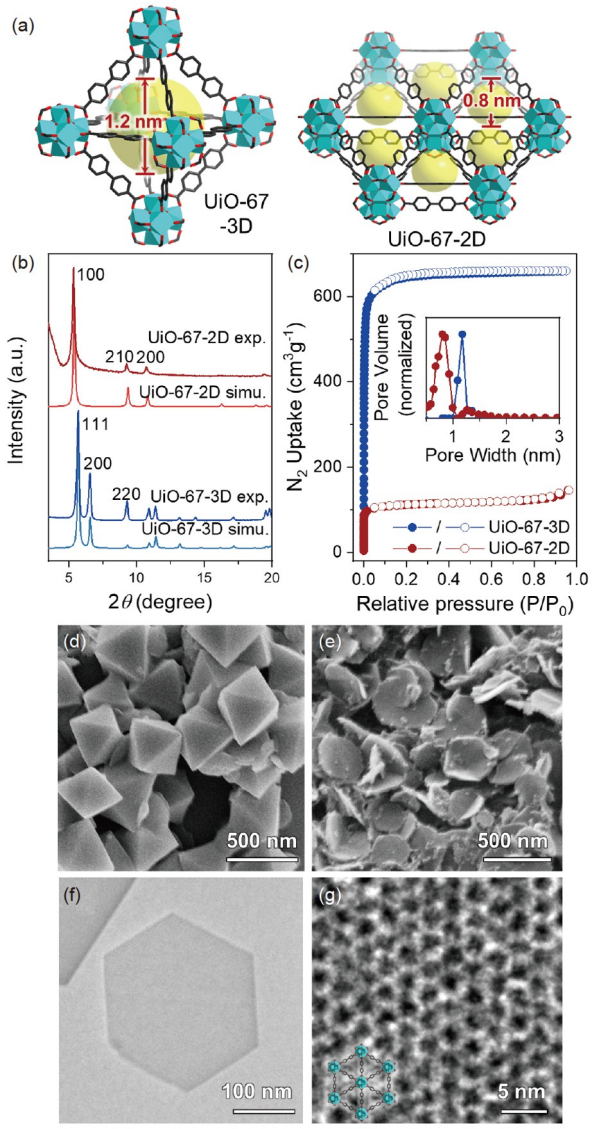

Figure 2 (a) Crystal structures of UiO-67-3D (left) and UiO-67-2D (right). Color scheme: Zr, blue polyhedral; O, red; C, black; MOF cavity, yellow sphere. (b) Experimental and simulated PXRD of UiO-67-3D and UiO-67-2D confirming the phase purity. (c) N_2 sorption isotherms at 77 K and pore size distributions derived from adsorption branches using a DFT model for UiO-67-3D and UiO-67-2D. SEM images of UiO-67-3D (d) and UiO-67-2D (e). TEM (f) and HR-TEM (g) images of UiO-67-2D. Inset shows the crystal structure of UiO-67-2D viewed along the *c*-axis (color online).

2D@Zn exhibits a steadily increasing overpotential from 18 to 49 mV (Figure 4b). Impressively, the overpotential of UiO-67-2D@Zn symmetric cells is better than those of most Zn anodes with various coatings, highlighting the distinct advantage of 2D-MOF coatings (Figure 4c) [18,38–41]. For comparison, UiO-67-3D@Zn symmetric cell exhibits voltage oscillations, while bare Zn-based cell has an abrupt rise in voltage at 3 mA cm^{-2} as a result of dendrite-caused short circuit (Figure 4a). The reduced overpotential of MOF-coated Zn anodes is attributed to the enhanced Zn^{2+} conductivity and reduced Zn nucleation barrier. First, the porous MOF coatings exhibit poor electronic conductivity, but good Zn^{2+} conductivity (Figure S2). The uniform Zn^{2+} diffusion channels of porous materials will regulate the diffusion of Zn^{2+} and reduce the mass transfer overpotential [26]. Second, the Zr-OH/H_2O sites on the surface of MOF particles act as zincophilic sites to effectively reduce the Zn nucleation potential, which will be discussed in later section. The long-term galvanostatic cycling performance of Zn, UiO-67-3D@Zn, and UiO-67-2D@Zn electrodes was further evaluated using symmetrical cells at 0.5 mA cm^{-2} (Figure 4d). Similar to the trend of rate performance, UiO-67-2D@Zn shows the highest stability and lowest overpotentials among the three electrodes, and operated for 850 h without obvious changes in overpotentials (Figure 4d inset). In contrast, UiO-67-3D-based Zn symmetric cells exhibit erratic voltage response with the gradually enlarged overpotential starting from 200 h, which is tentatively attributed to the protrusion of Zn dendrites through the loose UiO-67-3D layers. Bare Zn-based symmetric cells short-circuited after 71 h operation due to the dendrite puncturing through the separator. Furthermore, UiO-67-2D@Zn symmetric cell maintained fairly good stability at higher charging/discharging rate and capacity (150 h at 2 mA cm^{-2}, 2 mAh cm^{-2} (Figure S4a) and 60 h at 5 mA cm^{-2}, 5 mAh cm^{-2} (Figure S4b)), which is much higher than the UiO-67-3D@Zn and bare Zn symmetric cells. This was supported by the SEM and elemental mapping images. Cross-section SEM images after rate tests (0.25, 0.5, 1, 2, 3, 0.25 mA cm^{-2} for rate tests, each current density with 20 h cycle time) show the protrusion of Zn dendrites through the loose UiO-67-3D layers, whereas the dense UiO-67-2D layers remain intact. Elemental mappings further revealed the overlay of Zn and Zr elements within the UiO-67-3D layers, indicating the growth of Zn dendrites within the UiO-67-3D coatings (Figure S5a). In contrast, the Zn and Zr elements are well-separated on the UiO-67-2D/Zn interface, indicating the stability of UiO-67-2D coating to prevent Zn dendrites (Figure S5b). After rate tests (0.25, 0.5, 1, 2, 3, 0.25 mA cm^{-2} for rate tests, each current density with 20 h cycle time), the UiO-67-3D and UiO-67-2D coatings were further peeled off to show the morphology of the Zn surface. Unlike the dendrites and protuberance observed on bare Zn (Figure 5a) and UiO-67-3D@Zn (Figure 5b), the surface of UiO-67-2D-coated Zn remained smooth (Figure 5c). Therefore, the enhanced cycling stability of Zn anodes by MOF coatings can be attributed to the inhibition of dendrite growth. We further used PXRD to study the crystal orientation of deposited Zn on bare Zn, UiO-67-3D@Zn, and UiO-67-2D@Zn electrodes. Compared with the pristine Zn foil, the relative intensity of (002) peaks increased after deposition on bare Zn, UiO-67-3D@Zn, and UiO-67-2D@Zn electrodes, indicating the preferred growing along (002) direction (Figure S6). This is consistent with the growth of dendrites on bare Zn and UiO-67-3D@Zn electrodes after

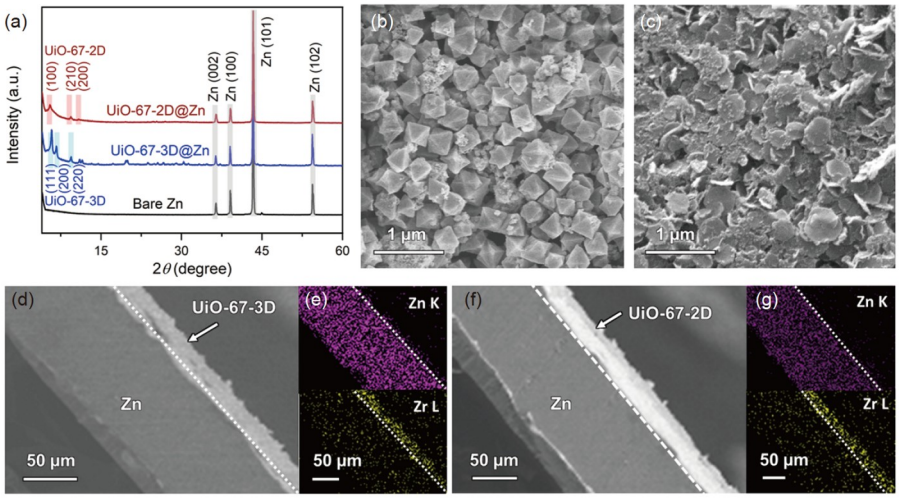

Figure 3 (a) PXRD of Zn, UiO-67-3D@Zn, and UiO-67-2D@Zn. Gray, blue, and yellow shadows highlight the characteristic peaks of Zn, UiO-67-3D, and UiO-67-2D. SEM images of UiO-67-3D@Zn (b) and UiO-67-2D@Zn (c). SEM cross-section images (d) and the corresponding EDS elemental mapping (e) of UiO-67-3D@Zn. SEM cross-section images (f) and the corresponding EDS elemental mapping (g) of UiO-67-2D@Zn (color online).

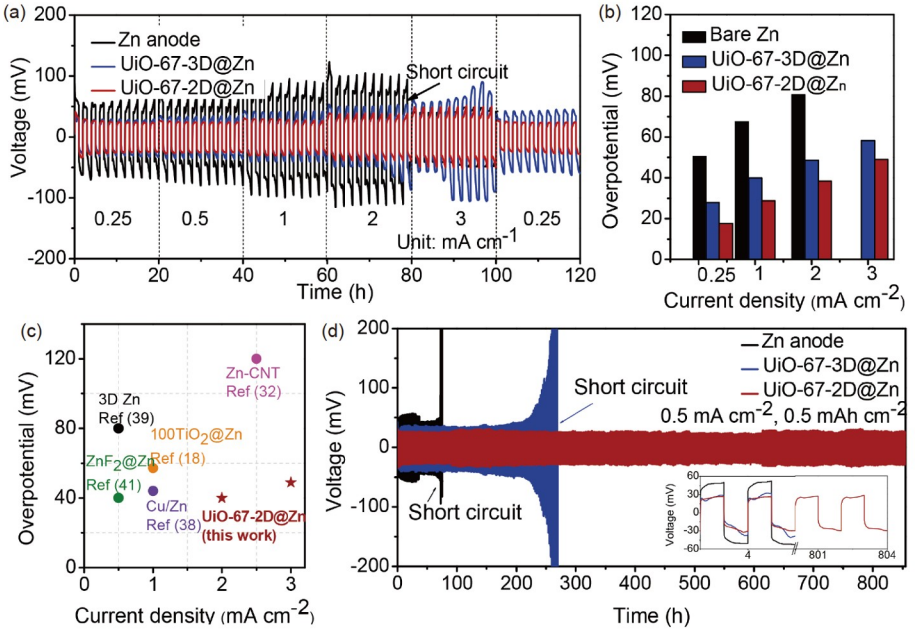

Figure 4 (a) Rate performance and (b) overpotential at different current densities for Zn, UiO-67-3D@Zn, and UiO-67-2D@Zn based symmetric cell. (c) Comparing overpotential of UiO-67-2D@Zn with that of surface-protected anodes in the literature. (d) Cycling stability of Zn-, UiO-67-3D@Zn-, and UiO-67-2D@Zn-based symmetric cell at 0.5 mA cm^{-2}, 0.5 mAh cm^{-2} (inset shows the expanded view at initial and final voltage profiles) (color online).

deposition. For comparison, the peak of (002) was much lower for UiO-67-2D@Zn electrode after deposition, which is in line with the inhibitory effects of UiO-67-2D nanoplates on dendrite formation. In addition, UiO-67-3D and UiO-67-2D were stable after multiple-cycle deposition, as confirmed by the maintained MOF diffraction peaks in PXRD patterns of UiO-67-3D@Zn and UiO-67-2D@Zn (Figure S7).

Linear polarization curves were collected to study the protective effect of MOF coatings against Zn corrosion in the electrolyte. The corrosion currents of bare Zn, UiO-67-3D @Zn and UiO-67-2D@Zn were 12.1, 4.9 and 0.44 μA cm^{-2}, respectively, with the corresponding voltages of −0.036, −0.023 and −0.021 V (Figure S8). The smaller corrosion current and positively shifted corrosion voltage indicate the anti-corrosion effect of MOF layers. *In-situ* optical microscope images were further adopted to monitor the H_2 evolution on different electrode surfaces. H_2 bubbles rapidly emerged on a bare Zn surface within 30 min, suggesting pronounced HER (Figure S9a). The UiO-67-2D and UiO-67-3D coatings alleviated the HER, as indicated by the clean surface after plating for 60 min (Figure S9b, c). *Ex-situ* optical micrographs in Figure S10 further show the dendrite

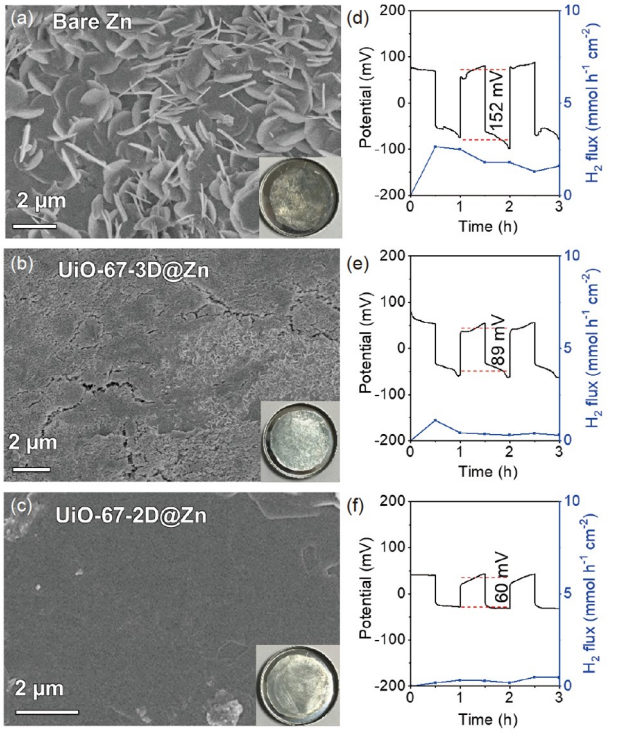

Figure 5 SEM images of bare Zn (a), UiO-67-3D@Zn (b) and UiO-67-2D@Zn (c) after rate tests by peeling off MOF coatings (0.25, 0.5, 1, 2, 3, 0.25 mA cm^{-2} for rate tests, each current density with 20 h cycle time). *In situ* monitoring of H_2 flux for symmetric cells of Zn//Zn (d), UiO-67-3D@Zn//UiO-67-3D@Zn (e), and UiO-67-2D@Zn//UiO-67-2D@Zn (f) by GC-MS (color online).

growth of bare Zn, UiO-67-3D@Zn, and UiO-67-2D@Zn after being plated in symmetric cells for 30 and 60 min at 1 mA cm^{-2}. To quantitate H_2 production during plating/stripping, we used *in situ* gas GC-MS to detect the H_2 flux of each electrode in 2 M $ZnSO_4$ using symmetric cells (3 mA cm^{-2}, 1.5 mAh cm^{-2}). The H_2 flux of bare Zn anodes in symmetric Zn//Zn cell reaches 2.6 mmol h^{-1} cm^{-2} during plating/stripping for 3 h (Figure 5d), while the UiO-67-3D@Zn (1.1 mmol h^{-1} cm^{-2}) and UiO-67-2D@Zn (0.5 mmol h^{-1} cm^{-2}) exhibit significantly reduced H_2 flux (Figure 5e, f). These results agree with the higher CE of UiO-67-2D measured using symmetric cells at a current density of 8.0 mA cm^{-2} and a capacity of 1.0 mAh cm^{-2} (Figure S11). The protective effect of MOF layers can be explained by their ability to separate water from Zn surface, which significantly reduced Zn corrosion and enhanced the stability. The better performance of UiO-67-2D@Zn than UiO-67-3D@Zn can be explained by the dense packing of UiO-67-2D nanosheets.

2.3 Mechanistic studies of Zn deposition

To mechanistically understand the effect of MOF coatings and explain the difference in protecting performances of UiO-67-3D and UiO-67-2D, DFT calculations were adopted. Considering the morphologies of nanoparticles, we used the most exposed crystal facets (111 for UiO-67-3D octahedral nanoparticles and 001 for UiO-67-2D nanoplates) to build our DFT models (Figure S12). The adsorption energy of Zn atoms on different sites of MOF/Zn interface was calculated to locate the preferred binding sites of Zn. Potential binding sites evaluated in the DFT calculation include the BPDC ligands (Figure 6b) and the Zr-OH/H_2O groups (Figure 6c). To compare the contribution of MOF coatings to Zn binding, the Zn adsorption energy on each site was referenced to the Zn adsorption energy on the bare Zn surface (Figure 6a). It was found that Zn preferentially bound to Zr-OH/H_2O (ΔG = −62.3 kJ mol^{-1}) over the BPDC ligand (ΔG = −37.1 kJ mol^{-1}) on the UiO-67-2D interface, which can be explained by the polar Zr-OH/H_2O groups favoring Zn binding. A similar trend was also observed for the UiO-67-3D interface (Table S1, Supporting Information online). Therefore, the Zr-OH/H_2O groups on the MOF/Zn interface act as strong Zn binding sites where Zn deposition initiates. This computational result is in line with the reduced overpotential of Zn plating (*i.e.*, lower nucleation barrier) by MOF coatings.

It should be noted that UiO-67-2D has a much higher Zr-OH/H_2O concentration than UiO-67-3D, which was verified by DRIFTS, TGA, and contact angle measurements. The peaks at 3,670 cm^{-1} can be assigned to the bridging μ_3-OH groups, while the broad band centered at 3,270 cm^{-1} corresponds to the hydrogen-bonded Zr-OH/H_2O (Figure 6d). UiO-67-2D shows a stronger adsorption band at 3,270 cm^{-1} than UiO-67-3D, indicating more Zr-OH/H_2O groups. The content of Zr-OH/H_2O was further quantified by TGA (Figure 6e). The weight losses at 300 and 550 °C are attributed to the removal of Zr-OH/H_2O and the framework decomposition, respectively. The weight loss of UiO-67-2D at ~350 °C (12.3 wt%) is significantly higher than that of UiO-67-3D (4.5 wt%), indicating a higher concentration of Zr-OH/H_2O. Further evidence was provided by contact angle measurements. The water contact angle of UiO-67-2D@Zn (55.1°, Figure 6h) is lower than that of UiO-67-3D@Zn (66.6°, Figure 6g) and bare Zn (87.9°, Figure 6f). Coating MOFs onto the Zn surface increased the hydrophilicity due to the hydrogen bond interactions between Zr-OH/H_2O groups and water molecules. The higher hydrophilicity of UiO-67-2D@Zn than UiO-67-3D@Zn indicates more Zr-OH/H_2O in UiO-67-2D. The different Zr-OH/H_2O concentrations in UiO-67-2D and UiO-67-3D originated from their structures and morphologies. UiO-67-3D is composed of coordinatively saturated $[Zr_6(\mu_3\text{-}O)_4(\mu_3\text{-}OH)_4](CO_2)_{12}$ clusters (Figure 6g inset), whereas UiO-67-2D contains a $[Zr_{12}(\mu_3\text{-}O)_8(\mu_3\text{-}OH)_8(\mu_2\text{-}OH)_6](OH)_6(H_2O)_6(CO_2)_{12}$ cluster with six pairs of terminal Zr-OH/H_2O (Figure 6h inset). In addition, the nanosheet morphology of UiO-67-2D shows exposed Zr-OH/H_2O on the (001) surface. Although terminal

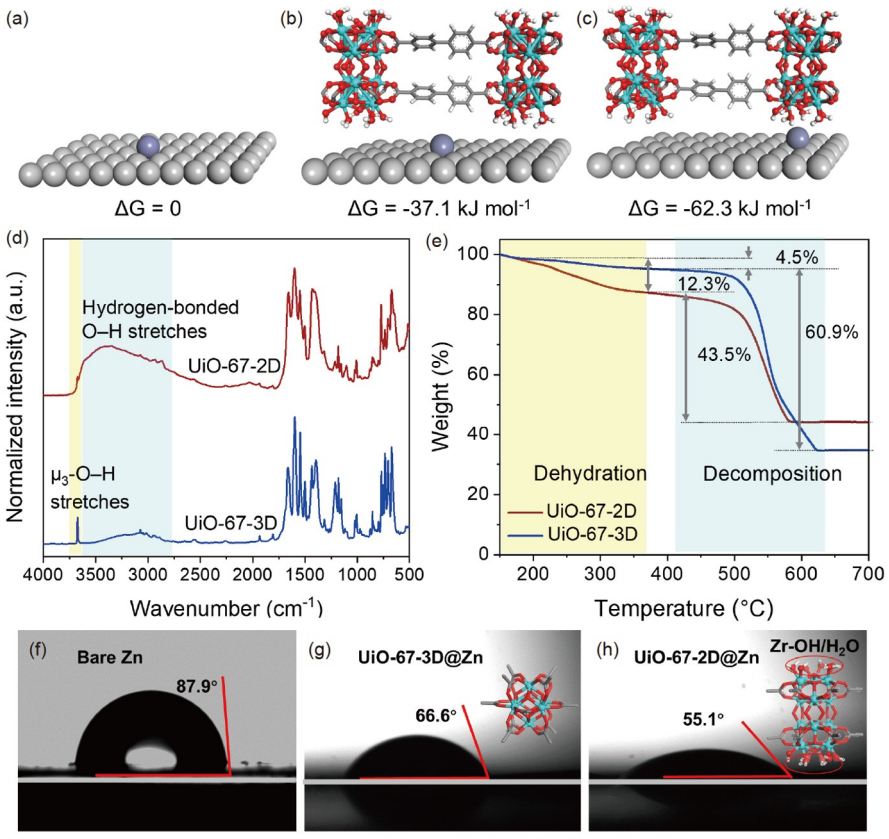

Figure 6 Structural model and corresponding adsorption energies of Zn on bare Zn (a), ligand sites of UiO-67-2D (b), and Zr-OH/H_2O sites of UiO-67-2D (c). (d) DRIFTS of UiO-67-2D and UiO-67-3D. Yellow and blue areas highlight the O–H stretches from μ_3-OH and hydrogen-bonded water. (e) TGA curves of UiO-67-2D and UiO-67-3D from room temperature (25 °C) to 700 °C at 10 °C min^{-1} under air flow. Yellow and blue areas highlight the dehydration of terminal Zr-OH/H_2O and decomposition of organic linkers of MOFs. Water contact angle measured for bare Zn (f), UiO-67-3D@Zn (g) and UiO-67-2D@Zn (h) (color online).

Zr-OH/H_2O also exists on the (111) surface of UiO-67-3D nanoparticles, the ratio of surface atoms in octahedral nanoparticles is expected to be lower than that of nanosheets. In summary, the higher cycling stability of UiO-67-2D@Zn than UiO-67-3D@Zn is attributed to the more exposed Zr-OH/H_2O as the zincophilic site, which induces uniform Zn deposition. Compared with octahedral nanoparticles of UiO-67-3D, the oriented UiO-67-2D nanosheets also ensure closer contact with the Zn surface to inhibit Zn dendrites and side reactions. The vertically aligned MOF channels further regulate Zn diffusion, leading to dendrite-free Zn deposition. These results highlighted the unique advantage of 2D MOF nanosheets as protective coatings for Zn anodes.

2.4 Full cell performance

To further evaluate the performance of MOF@Zn anodes in practical ZIBs, Mn_2O_3/C nanoflakes derived from Mn-MOF were employed as the cathode materials to assemble MOF@Zn||Mn_2O_3/C cells. Mn_2O_3/C cathode was derived from Mn-MOF, and it displayed a nanoflake structure. The corresponding mapping shows that C, Mn, and O are uniformly distributed (Figure S13). Raman spectrum of Mn_2O_3/C manifests the D band at 1,340 cm^{-1}, G band at 1,599 cm^{-1}, and I_G/I_D of 1.43, indicating the graphitic carbon (Figure S14a). The spin-orbit splitting value from XPS of Mn_2O_3/C is 11.3 eV, which matches that of Mn_2O_3. The peaks of Mn $2p_{1/2}$ at 651.53 eV and Mn $2p_{3/2}$ at 639.9 eV belong to Mn^{2+}. Mn $2p_{1/2}$ at 651.59 eV and Mn$2p_{3/2}$ at 641.0 eV are attributed to Mn^{3+}. Mn $2p_{1/2}$ at 653.05 eV and Mn $2p_{3/2}$ at 642.4 eV are assigned to Mn^{4+}. Shake-up peaks are situated at 644.8 eV (Figure S14c). The O 1s peak at 529 eV is from surface lattice oxygen, that at 531.3 eV is due to adsorbed oxygen, and that at 533.0 eV was attributed to adsorbed water (Figure S14d). N_2 adsorption and desorption curve and pore size distribution indicate a specific surface area of 265 m^2 g^{-1} and a pore size of approximately 10 nm (Figure S14e). PXRD patterns of Mn-MOF and Mn_2O_3/C are consistent with simulations, confirming the phase purity (Figure S14f) [42]. The ZIBs were tested in electrolytes containing 2 M $ZnSO_4$ and 0.1 M $MnSO_4$ (Figures S15, S16a). EIS shows that the bulk resistance of MOF-coated Zn full cell is larger than that of bare Zn, possibly due to the poor electrical conductivity of MOF coatings. However, the higher slope in the low-frequency region for MOF-coated full cells indicates faster Zn^{2+} diffusion, which is consistent with the high Zn^{2+} conductivity

of MOF coatings. The cyclic voltammetry (CV) curves of the ZIBs with different anodes (Figure S16b) display identical redox peaks, proving the negligible impact of MOF coating on Zn^{2+} diffusion in ZIBs [43]. The slightly smaller voltage polarization of UiO-67-2D@Zn||Mn_2O_3/C cathode reveals its better reversibility than that of UiO-67-3D@Zn and bare Zn, possibly due to the lower Zn nucleation barrier on the Zr-OH/H_2O sites. ZIBs with different anodes also display similar galvanostatic charge-discharge (GCD) curves, and UiO-67-2D@Zn||Mn_2O_3/C, UiO-67-3D@Zn||Mn_2O_3/C, and Zn||Mn_2O_3/C ZIBs achieve the capacities of 240, 212 and 210 mAh g^{-1} at 1 A $g^{-1,}$ respectively (Figure S16c). Rate capability tests show that the specific capacity of UiO-67-2D@Zn||Mn_2O_3/C gradually decreases as the current density increases (Figure S17), but the capacity is fully recovered to 240 mAh g^{-1} when the cycling rate is switched back to 1 A g^{-1}. However, the capacity of UiO-67-3D@Zn||Mn_2O_3/C and Zn||Mn_2O_3/C ZIBs exhibits a quick decay with current densities increasing to 5 A g^{-1}. When switched back to 1 A g^{-1}, they were unable to reach the initial level, indicating an inferior rate performance due to high charge transfer resistance (Figure S16d). More importantly, UiO-67-2D@Zn||Mn_2O_3/C shows high cycling stability with 81% retention of initial capacitance and a CE of nearly 100% after 1,500 cycles at 2 A g^{-1} (Figure S16e), which is more stable than that of UiO-67-3D@Zn (64% capacitance retention) and bare Zn-based ZIBs (42% capacitance retention). To display the practical application of ZIBs, UiO-67-2D@Zn||Mn_2O_3/C lighted up 12 light-emitting diodes (LEDs) and a digital watch (Figures S16e inset).

3 Conclusions

In conclusion, UiO-67-2D and UiO-67-3D were applied as Zn anodes to investigate the impact of MOF structures and morphologies on the cycling performance of Zn anodes. Compared with UiO-67-3D@Zn, the enhanced performance of the UiO-67-2D@Zn anode was attributed to the higher concentration of Zr-OH/H_2O as zincophilic sites to induce uniform Zn deposition. The nanosheet morphology further ensured close contact with the Zn surface, which prevents HER reactions while permitting Zn^{2+} diffusion through the perpendicularly aligned channels. The UiO-67-2D@Zn||Mn_2O_3/C cell achieves high capacity (240 mAh g^{-1} at 1 A g^{-1}), good rate performance and cycling stability (81% capacity retention after 1,500 cycles at 2 A g^{-1}). This unique Zn anode design using 2D MOF coatings not only provided a promising anode candidate for ZIBs, but also related the MOF structures/morphologies to the performance of protected Zn anodes. This mechanistic understanding of the structure-property relationship will guide the design of protective materials for Zn anodes. Future work will focus on the surface engineering of MOF nanosheets by polar functional groups to tune Zn deposition and further enhance Zn anode stability. Furthermore, considering the precisely controllable surface structures and pore environments of MOFs, surface coatings with high stability and Zn^{2+} ionic conductivity can be envisioned for advanced aqueous zinc ion batteries.

Acknowledgements This work was supported by the National Natural Science Foundation of China (52178219). We acknowledge the helpful discussions with Dr. Yunguang Zhu (Research Laboratory of Electronics, Massachusetts Institute of Technology). We thank Shijia Feng, Yiding Jiao, and Fangyan Li (College of Engineering and Applied Sciences, Nanjing University) for their kind help with GC-MS and optical microscopy measurements.

Conflict of interest The authors declare no conflict of interest.

Supporting information The supporting information is available online at http://chem.scichina.com and http://link.springer.com/journal/11426. The supporting materials are published as submitted, without typesetting or editing. The responsibility for scientific accuracy and content remains entirely with the authors.

1 Sun W, Wang F, Hou S, Yang C, Fan X, Ma Z, Gao T, Han F, Hu R, Zhu M, Wang C. *J Am Chem Soc*, 2017, 139: 9775–9778
2 Wang F, Borodin O, Gao T, Fan X, Sun W, Han F, Faraone A, Dura JA, Xu K, Wang C. *Nat Mater*, 2018, 17: 543–549
3 Xu C, Li B, Du H, Kang F. *Angew Chem*, 2012, 124: 957–959
4 Cui Y, Zhao Q, Wu X, Chen X, Yang J, Wang Y, Qin R, Ding S, Song Y, Wu J, Yang K, Wang Z, Mei Z, Song Z, Wu H, Jiang Z, Qian G, Yang L, Pan F. *Angew Chem*, 2020, 132: 16737–16744
5 Fang G, Zhou J, Pan A, Liang S. *ACS Energy Lett*, 2018, 3: 2480–2501
6 Zhao J, Zhang J, Yang W, Chen B, Zhao Z, Qiu H, Dong S, Zhou X, Cui G, Chen L. *Nano Energy*, 2019, 57: 625–634
7 Pan H, Ellis JF, Li X, Nie Z, Chang HJ, Reed D. *ACS Appl Mater Interfaces*, 2019, 11: 37524–37530
8 Qiu X, Wang N, Wang Z, Wang F, Wang Y. *Angew Chem Int Ed*, 2021, 60: 9610–9617
9 Parker JF, Chervin CN, Pala IR, Machler M, Burz MF, Long JW, Rolison DR. *Science*, 2017, 356: 415–418
10 Zheng J, Zhao Q, Tang T, Yin J, Quilty CD, Renderos GD, Liu X, Deng Y, Wang L, Bock DC, Jaye C, Zhang D, Takeuchi ES, Takeuchi KJ, Marschilok AC, Archer LA. *Science*, 2019, 366: 645–648
11 Li Q, Zhao Y, Mo F, Wang D, Yang Q, Huang Z, Liang G, Chen A, Zhi C. *EcoMat*, 2020, 2: e12035
12 Li C, Xie X, Liang S, Zhou J. *Energy Environ Mater*, 2020, 3: 146–159
13 Yang Q, Li Q, Liu Z, Wang D, Guo Y, Li X, Tang Y, Li H, Dong B, Zhi C. *Adv Mater*, 2020, 32: 2001854
14 Blanc LE, Kundu D, Nazar LF. *Joule*, 2020, 4: 771–799
15 Zhao Z, Zhao J, Hu Z, Li J, Li J, Zhang Y, Wang C, Cui G. *Energy Environ Sci*, 2019, 12: 1938–1949
16 Li H, Xu C, Han C, Chen Y, Wei C, Li B, Kang F. *J Electrochem Soc*, 2015, 162: A1439–A1444
17 Liang P, Yi J, Liu X, Wu K, Wang Z, Cui J, Liu Y, Wang Y, Xia Y, Zhang J. *Adv Funct Mater*, 2020, 30: 1908528
18 Zhao K, Wang C, Yu Y, Yan M, Wei Q, He P, Dong Y, Zhang Z, Wang X, Mai L. *Adv Mater Interfaces*, 2018, 5: 1800848
19 He H, Tong H, Song X, Song X, Liu J. *J Mater Chem A*, 2020, 8: 7836–7846
20 Bhoyate S, Mhin S, Jeon JE, Park KR, Kim J, Choi W. *ACS Appl Mater Interfaces*, 2020, 12: 27249–27257

21 Li W, Wang K, Zhou M, Zhan H, Cheng S, Jiang K. *ACS Appl Mater Interfaces*, 2018, 10: 22059–22066
22 Li B, Xue J, Han C, Liu N, Ma K, Zhang R, Wu X, Dai L, Wang L, He Z. *J Colloid Interface Sci*, 2021, 599: 467–475
23 Kim JY, Liu G, Shim GY, Kim H, Lee JK. *Adv Funct Mater*, 2020, 30: 2004210
24 Yuan S, Feng L, Wang K, Pang J, Bosch M, Lollar C, Sun Y, Qin J, Yang X, Zhang P, Wang Q, Zou L, Zhang Y, Zhang L, Fang Y, Li J, Zhou HC. *Adv Mater*, 2018, 30: 1704303
25 Pu X, Jiang B, Wang X, Liu W, Dong L, Kang F, Xu C. *Nano-Micro Lett*, 2020, 12: 152
26 Liu X, Yang F, Xu W, Zeng Y, He J, Lu X. *Adv Sci*, 2020, 7: 2002173
27 Wang Z, Huang J, Guo Z, Dong X, Liu Y, Wang Y, Xia Y. *Joule*, 2019, 3: 1289–1300
28 Yuksel R, Buyukcakir O, Seong WK, Ruoff RS. *Adv Energy Mater*, 2020, 10: 1904215
29 Chen K, Guo H, Li W, Wang Y. *ACS Appl Mater Interfaces*, 2021, 13: 54990–54996
30 Cao L, Li D, Deng T, Li Q, Wang C. *Angew Chem Int Ed*, 2020, 59: 19292–19296
31 Liu M, Yang L, Liu H, Amine A, Zhao Q, Song Y, Yang J, Wang K, Pan F. *ACS Appl Mater Interfaces*, 2019, 11: 32046–32051
32 Yang H, Chang Z, Qiao Y, Deng H, Mu X, He P, Zhou H. *Angew Chem Int Ed*, 2020, 59: 9377–9381
33 Wang Y, Liu Y, Wang H, Dou S, Gan W, Ci L, Huang Y, Yuan Q. *J Mater Chem A*, 2022, 10: 4366–4375
34 Cavka JH, Jakobsen S, Olsbye U, Guillou N, Lamberti C, Bordiga S, Lillerud KP. *J Am Chem Soc*, 2008, 130: 13850–13851
35 Cliffe MJ, Castillo-Martínez E, Wu Y, Lee J, Forse AC, Firth FCN, Moghadam PZ, Fairen-Jimenez D, Gaultois MW, Hill JA, Magdysyuk OV, Slater B, Goodwin AL, Grey CP. *J Am Chem Soc*, 2017, 139: 5397–5404
36 Dai R, Peng F, Ji P, Lu K, Wang C, Sun J, Lin W. *Inorg Chem*, 2017, 56: 8128–8134
37 Wang Z, Hu J, Han L, Wang Z, Wang H, Zhao Q, Liu J, Pan F. *Nano Energy*, 2019, 56: 92–99
38 Cai Z, Ou Y, Wang J, Xiao R, Fu L, Yuan Z, Zhan R, Sun Y. *Energy Storage Mater*, 2020, 27: 205–211
39 Kang Z, Wu C, Dong L, Liu W, Mou J, Zhang J, Chang Z, Jiang B, Wang G, Kang F, Xu C. *ACS Sustain Chem Eng*, 2019, 7: 3364–3371
40 Li M, He Q, Li Z, Li Q, Zhang Y, Meng J, Liu X, Li S, Wu B, Chen L, Liu Z, Luo W, Han C, Mai L. *Adv Energy Mater*, 2019, 9: 1901469
41 Han J, Euchner H, Kuenzel M, Hosseini SM, Groß A, Varzi A, Passerini S. *ACS Energy Lett*, 2021, 6: 3063–3071
42 Bao L, Sun FZ, Zhang GY, Hu TL. *ChemSusChem*, 2020, 13: 548–555
43 Zhang N, Huang S, Yuan Z, Zhu J, Zhao Z, Niu Z. *Angew Chem Int Ed*, 2021, 60: 2861–2865